

Three-phase interface engineering via P-doped CoMo₂S₄-integrated Co₄S₃/Co₂P enables high-efficiency overall water splitting

Kaixuan Dong ^a, Duy Thanh Tran ^{a, **}, Xue Li ^a, Sampath Prabhakaran ^a, Do Hwan Kim ^b, Nam Hoon Kim ^{a,c}, Joong Hee Lee ^{a,c,d,*}

^a Department of Nano Convergence Engineering, Jeonbuk National University, Jeonju, Jeonbuk 54896, Republic of Korea

^b Division of Science Education, Department of Energy Storage/Conversion Engineering, Jeonbuk National University, Jeonju-si, Jeonbuk 54896, Republic of Korea

^c AHES Co., 445 Techno Valley-ro, Bongdong-eup, Wanju-gun, Jeonbuk, Republic of Korea

^d Carbon Composite Research Center, Department of Polymer-Nano Science and Technology, Jeonbuk National University, Jeonju, Jeonbuk 54896, Republic of Korea

ARTICLE INFO

Keywords:

Three-phase interface
P-doped CoMo₂S₄-integrated Co₂P/Co₄S₃
High-performance catalyst
Overall water splitting

ABSTRACT

In this research, we constructed a three-phase interface derived from phosphorous-doped CoMo₂S₄ sheets integrated Co₂P/Co₄S₃ hybrid heterostructure (P – CoMo₂S₄/Co₄S₃–Co₂P) to form a high-efficiency electrocatalyst, which can promote both hydrogen and oxygen evolution in alkaline electrolyte. To attain a current density of 10 mA cm⁻², P – CoMo₂S₄/Co₄S₃–Co₂P requires an overpotential of only 54 mV for cathodic reaction, and 296 mV for anodic reaction. A two-electrode electrolyzer of P – CoMo₂S₄/Co₄S₃–Co₂P_(+, -) shows a low cell voltage of 1.55 V at 10 mA cm⁻² and prospective durability of 95.6% performance retention after 50 h. Furthermore, a solar energy-powered water electrolysis system reveals an effective solar-to-hydrogen efficiency of 14.1%. The high catalytic performances are well understood by experiment and theoretical studies, which indicate the enhanced electroactive surface, rapid charge transfer, and optimum adsorption energy for promoting well the reaction kinetics. The achievements provide a promising high-performance electrocatalyst for green hydrogen generation by water splitting.

1. Introduction

As a consequence of human activity, Earth's environment is facing a multitude of challenges relating to climate change and pollution resulting from the excessive consumption of various fossil fuels. Therefore, it is necessary to develop eco-friendly alternatives and renewable energy sources. Among potential candidates, hydrogen gas has emerged as a promising option due to its renewability, cleanness, and high energy density advantages [1]. One of the most efficient methods for producing green hydrogen is the electrochemical water splitting process [2]; however, the limited reaction kinetics for the reactions of hydrogen evolution (HER) at cathodic electrode and oxygen evolution (OER) at anodic electrode [3], as well as the required use of expensive and scarce noble metal-based catalysts at these cathode and anode electrodes, present critical challenges [4,5]. Therefore, the design of effective noble metal-free catalysts to promote both HER and OER is currently attracted great attention [6–8]. Through specific macro/micro/nano engineering approaches, various catalyst candidates have been designed with unique

stable structure and high activities [9,10]. However, to further improve catalytic performance to reach practical possibility, the active site number and current conductivity of catalysts must be enhanced. Early reported studies reveal that the formation of core-shell heterostructures under a hierarchical three-dimensional (3D) architecture is attracting widespread attention for creating high density of catalyst sites, and uniform and adjustable pore sizes with diverse conductive channels and fast mass diffusion to upgrade catalytic performance [11,12]. Among various developed materials, well-defined mesoporous multi-metallic sulfide architectures, such as CoMoS or NiMoS, have been demonstrated as potential candidates for cutting-edge electrochemical applications [13–21]. In particular, the synthesis of heterostructures based on them further highlights the advantage of synthesizing a network of pores, surface areas, and multiple active centers, thus increasing the catalytic performance of both OER and HER. In this context, Guo et al. developed mesoporous material of MoS₂/CoMo₂S₄ heterostructures, which enable rapid charge transfer ability, excellent mass/gas diffusion, and improved electronic properties, thereby resulting in excellent

* Corresponding author at: Department of Nano Convergence Engineering, Jeonbuk National University, Jeonju, Jeonbuk 54896, Republic of Korea.

** Corresponding author.

E-mail addresses: dttran@jbnu.ac.kr (D.T. Tran), jhl@jbnu.ac.kr (J.H. Lee).



activities toward both HER and OER [14]. Recently, Song et al. explored the bifunctional electrocatalyst derived from a novel free-standing $\text{Co}_3\text{S}_4/\text{CoMo}_2\text{S}_4$ heterostructure, which allows the formation of a heterogeneous $\text{Co}_3\text{S}_4-\text{CoMo}_2\text{S}_4$ interface to give rich active sites and good conductivity to boost the catalytic performances [22]. Nguyen et al. designed a hybrid of small $\text{CoS}_x@\text{Cu}_2\text{MoS}_4$ particles dispersed on $\text{MoS}_2/\text{N},\text{S}$ -doped graphene, which can offer unique multi-combined active centers, as well as synergistic effects to facilitate OER and HER in alkaline electrolyte [23]. In addition, several studies realized that since the multi-metallic sulfide architectures are doped with specific heteroatoms, their electronic structure may be well adjusted to efficiently adsorb/desorb reactants/intermediates, thus showing high priority for hydrogen production [24–27]. Despite some exciting achievements being reported, it is widely realized that the reactivity, stability, and conductivity of the multi-metallic sulfides should be further boosted to meet and surpass the commercial targets of practical electrocatalysts toward water electrolysis application. Therefore, in this research, we successfully synthesize a 3D hierarchical core-shell hybrid architecture based on the in-situ growth of P-doped CoMo_2S_4 nanosheets coupled $\text{Co}_2\text{P}/\text{Co}_4\text{S}_3$ structures ($\text{P} - \text{CoMo}_2\text{S}_4/\text{Co}_4\text{S}_3-\text{Co}_2\text{P}$) carried by a nickel foam (NF) substrate, as a high-efficiency catalyst for bifunctionally boosting the HER and OER processes. The catalyst acts as a binder-free self-supporting electrode with excellent physicochemical properties of huge specific surface area, abundance of active centers, and outstanding electrical conductivity, which are achieved through unique multi-interfacial engineering and core-shell heterostructure design. These features allow the material to require a low cell voltage and provide an excellent durability toward a cost-effective and robust water splitting process to produce green hydrogen gas.

2. Experimental section

2.1. Materials

Potassium hydroxide pellets (KOH, 85%), ethanol ($\text{C}_2\text{H}_5\text{OH}$, 99%), and hydrochloric acid (HCl, 37.5 wt%) were purchased from Samchun Co., Ltd. (Korea). Cobalt(II) nitrate hexahydrate ($\text{Co}(\text{NO}_3)_2 \cdot 6 \text{ H}_2\text{O}$, ≥ 98.0%), sodium hypophosphite monohydrate ($\text{NaH}_2\text{PO}_2 \cdot \text{H}_2\text{O}$, 99.9%), ammonium fluoride (NH_4F , ≥ 98.0%), Pt on two-dimensional graphitized carbon layer (Pt/C, 20 wt%), urea ($\text{Co}(\text{NH}_2)_2$, ≥ 99.5%), sodium molybdate dihydrate ($\text{Na}_2\text{MoO}_4 \cdot 2 \text{ H}_2\text{O}$, 99.99%), thiourea ($\text{CH}_4\text{N}_2\text{S}$, 99.0%), RuO_2 (99.9%), and a solution of 5 wt% nafion were obtained from Sigma-Aldrich Chemicals Co., Ltd. (USA).

2.2. Synthesis of the Co_2P material

A nickel foam (NF) substrate was first cleaned for 20 min by dipping in 3.0 M HCl, followed by dipping into deionized (DI) water and ethanol several times. After that, the NF was placed in a Teflon autoclave containing a solution of 25 mmol of $\text{Co}(\text{NH}_2)_2$, 5 mmol of $\text{Co}(\text{NO}_3)_2 \cdot 6 \text{ H}_2\text{O}$, and 10 mmol of NH_4F in 80 mL of DI water, to conduct a hydrothermal process at 120 °C for 5 h. After completing the reaction, the achieved sample was collected, washed several times with DI water and ethanol, followed by drying overnight at 60 °C. Subsequently, it was kept in quartz boat in a CVD heating system to conduct a phosphidization reaction at 350 °C for 2 h with the flow of Ar gas (100 sccm) at a heating rate of approximately $2 \text{ }^{\circ}\text{C min}^{-1}$, and the use of 1.0 g of $\text{NaH}_2\text{PO}_2 \cdot \text{H}_2\text{O}$ as a phosphorous source.

2.3. Synthesis of the $\text{CoMo}_2\text{S}_4/\text{Co}_4\text{S}_3-\text{Co}_2\text{P}$ and $\text{P} - \text{CoMo}_2\text{S}_4/\text{Co}_4\text{S}_3-\text{Co}_2\text{P}$ material

In a specific process, a sample of Co_2P NWs/NF was kept in Teflon autoclave containing 30 mL solution of $\text{Na}_2\text{MoO}_4 \cdot 2 \text{ H}_2\text{O}$ (0.3 g) and thiourea (0.33 g), to be subjected to a hydrothermal process at 200 °C for 8 h. After completing the reaction, the obtained sample was washed with

DI water/ethanol 3 times, then dried at 60 °C overnight. Subsequently, a sample of the $\text{CoMo}_2\text{S}_4/\text{Co}_4\text{S}_3-\text{Co}_2\text{P}$ was placed in a quartz boat to enable another phosphidization step at 300 °C under a heating rate of $3 \text{ }^{\circ}\text{C min}^{-1}$, an Ar flow of 100 sccm, along with the use of 200 mg $\text{NaH}_2\text{PO}_2 \cdot \text{H}_2\text{O}$ as a phosphorous precursor source. After the reaction took place for 1 h, the reactor was cooled to ambient environment, and the product of $\text{P} - \text{CoMo}_2\text{S}_4/\text{Co}_4\text{S}_3-\text{Co}_2\text{P}$ was collected for further characterizations (Fig. 1).

2.4. Materials characterizations

The morphology and structure of the synthesized materials were analyzed thorough field-emission scanning electron microscopy (FE-SEM) together with energy dispersive spectroscopy (EDS) using a Supra 40 VP instrument (Zeiss Co., Germany) at the Center for University-wide Research Facilities, Jeonbuk National University (South Korea). In addition, transmission electron microscopy (TEM) and high-resolution TEM (HR-TEM) via a JEM-ARM200F instrument from JEOL Co. (Japan) at the KBSI center in Jeonju (South Korea) were also employed for microstructural analysis of the materials. To ascertain the phase composition of the materials, X-ray diffraction (XRD) test was conducted over a range of (5 to 85) degrees on a Rigaku D/max 2400 X-ray generator with applied $\text{Cu}-\text{K}\alpha$ radiation ($\lambda = 0.154 \text{ nm}$). Chemical state of the synthetic candidates were determined through X-ray photoelectron spectroscopy (XPS) via a Theta Probe instrument (Thermo Fisher Scientific, Inc., USA.). Furthermore, to evaluate surface area and porosity of those materials, an ASAP 2020 Plus system (Micromeritics Instrument Corp., USA.) was employed. In this context, a suitable powder amount of the active material was collected by gently scraping from NF substrate and then used to measure specific surface area via the Brunauer–Emmett–Teller (BET) theoretical model and pore volume via the Barrett–Joyner–Halenda (BJH) theoretical model.

2.5. Electrochemical characterizations

To assess the catalytic performances, the synthesized materials-based working electrode (1 cm × 1 cm), graphite bar-based counter electrode, and Ag/AgCl reference electrode were employed for different electrochemical characterizations. A comprehensive series of electrochemical measurements were performed using a CHI660D electrochemical workstation (CH Instruments Inc., USA.) in 1.0 M KOH aqueous solution under ambient room temperature condition. We acquired linear-sweep voltammetry (LSV) profiles for both HER and OER in a three-electrode system at a potential sweep rate of 2 mV s^{-1} . An iR-corrected process of 100% was applied to the achieved LSV results. To determine the double-layer capacitance (C_{dl}), which is well consistent with the electrochemical surface area (ECSA), we analyzed the current difference at various scanning speeds of (5, 10, 20, 40, 60, 80, and 100) mV s^{-1} via cyclic voltammetry (CV) in a region of non-Faradaic reaction. The electrochemical impedance spectrum (EIS) tests for the materials were used to determine their charge transfer resistance. In addition, the chronopotentiometry technique was applied to reveal their durability. The potential value obtained from electrochemical measurements was transformed from vs. Ag/AgCl into vs. reversible hydrogen electrode (vs. RHE) by the followed equation:

$$\text{E/V (vs-RHE)} = \text{E}_{\text{Ag/AgCl}} + 0.0591 \times \text{pH} + 0.197 \quad (1)$$

Commercial catalysts, including Pt/C and RuO_2 -based electrodes, were utilized to compare with our synthetic materials for HER and OER activities, respectively. The Pt/C or RuO_2 -based electrode was prepared by dispersing 5 mg of Pt/C (or RuO_2) powder into 500 μL ethanol containing 30 μL Nafion to create a homogeneous ink under the assistance of sonication process, which was subsequently deposited on the NF surface (1 cm × 1 cm), and then dried overnight at 60 °C.

The water splitting activity of two-electrolyzer cell derived from the

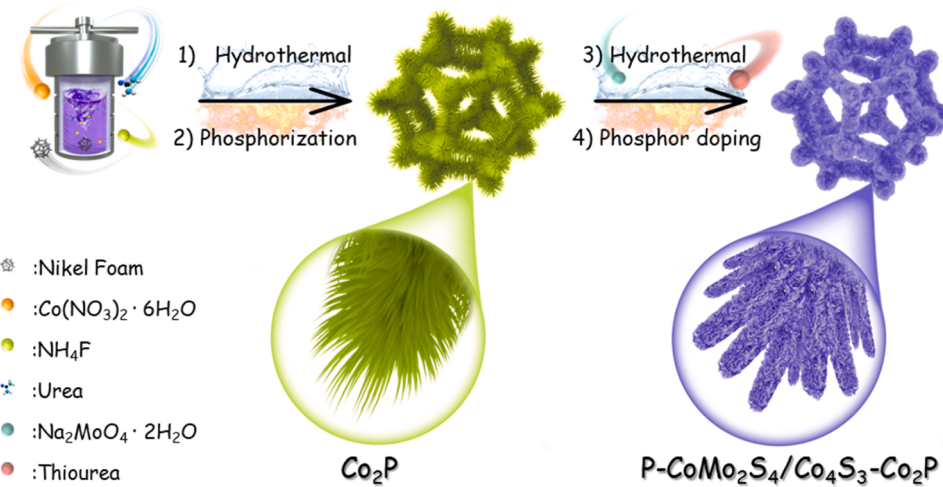


Fig. 1. Schematic of the preparation of the P – CoMo₂S₄/Co₄S₃-Co₂P material on NF substrate.

P – CoMo₂S₄/Co₄S₃-Co₂P_(+,-) or Pt/C₍₋₎//RuO₂₍₊₎ was assessed by LSV in 1.0 M KOH at a sweep rate of 2.0 mV s⁻¹. The Faraday efficiency was evaluated by comparing the collected volumes of H₂ and O₂ generated during the reaction with the theoretical hydrogen and oxygen volumes evolved with the assumption of 100% use of the current input for the catalytic reactions. A solar energy-powered water electrolysis system, consisting of the P – CoMo₂S₄/Co₄S₃-Co₂P_(+,-) and a solar cell panel (5 cm × 5 cm) having an effective surface area of 11.55 cm², was tested by irradiation from a HAL-320 solar simulator (Asahi Spectra Co., Ltd., Japan). The following equation was applied to calculate the solar-to-hydrogen (STH) efficiency of the system [28]:

$$\text{STH \%} = (J \times 1.23 \text{ V}) / 100 \text{ mW cm}^{-2} \quad (2)$$

Where, J is the current density from the intersection point between the LSV curve of the water splitting process and J-V curve of the solar cell; value of 100 mW cm⁻² is the power density of the simulated solar light.

3. Results and discussion

3.1. Structural characterizations

Fig. 1 shows a schematic of the fabrication of the 3D hierarchical P – CoMo₂S₄/Co₄S₃-Co₂P catalyst, which began with the growth of one-dimensional Co₂P NWs with a uniform diameter of ~100 nm and length of several micrometers on the NF (**Fig. S1**) via the hydrothermal reaction, followed by a phosphidization process. The Co₂P NWs on NF show good crystalline structure (ICSD #98–010–7550) (**Fig. S2**) and generate an increase of specific surface area to provide high potential for supporting active materials to achieve large active surface area and high electron transfer ability [29]. A subsequent hydrothermal reaction was successfully conducted to produce a Co₂P–Co₄S₃ heterostructure, as well as generate a nanolayer of CoMo₂S₄ sheets uniformly coating the Co₂P–Co₄S₃ surface at the same time, thereby significantly increasing the diameter of NWs, which also achieve an average diameter of ~200 nm and highly porous morphology (**Fig. S3**). To further adjust the electronic properties of the CoMo₂S₄ material, a second phosphidization treatment was applied to insert low loading phosphorus into its structure, thus forming a final product of P – CoMo₂S₄/Co₄S₃-Co₂P with a well-maintained morphology that was consistent with that of CoMo₂S₄/Co₄S₃-Co₂P. **Fig. 2a–c** show an abundance of vertical CoMo₂S₄-P NSs having a thickness of ~10 nm fully covering the Co₂P–Co₄S₃ surface, to form a highly wrinkled 3D structure. The TEM image of **Fig. 2d** further confirms the formation of a core–shell structure, in which a gray outer layer of ~50 nm thickness enwraps a black core of ~100 nm diameter.

The high-resolution TEM images in **Fig. 2e–f** show insight into the structure of an interface area, which displays the existence of CoMo₂S₄ phase with a corresponding lattice fringe of 0.572 nm from the (002) crystal plane at the shell (**Fig. 2f1**), Co₂P phase with a corresponding lattice fringe of 0.221 nm from the (121) crystal plane (**Fig. 2f2**), and Co₄S₃ phase with a corresponding lattice fringe of 0.182 nm from the (220) crystal plane (**Fig. 2f3**) at the core part.

The STEM–EDS color mapping (**Fig. 2g**) and line-scan mapping (**Fig. S4**) reveal the respective signal distribution of Co, Mo, P, and S elements with their content of approximately 26.6, 16.9, 42.6, and 13.9 wt%, respectively. **Fig. 2h** shows the crystallinity of the as-synthesized materials that was studied by XRD analysis. The XRD pattern of the P – CoMo₂S₄/Co₄S₃-Co₂P catalyst well indicates the crystalline characteristics of CoMo₂S₄ phase (JCPDS #024–0332), Co₄S₃ phase (JCPDS #019–0363), and Co₂P phase (ICSD #98–010–7550), and matched well with the obtained TEM results, thus providing evidence of the P – CoMo₂S₄/Co₄S₃-Co₂P heterostructure. Excitingly, the crystal deformation caused by the interface formation and doping effect is clearly observed in **Fig. 2i** and j, which reveal a significant downshift of the (121) peak from Co₂P and (002) peak from CoMo₂S₄ phases of the P – CoMo₂S₄/Co₄S₃-Co₂P material, as compared to those of the CoMo₂S₄/Co₄S₃-Co₂P and Co₄S₃-Co₂P. This is consistent with a strain phenomenon for the Co₂P and CoMo₂S₄ structures resulting from the strong core–shell interactions as well as crystalline mismatch due to the difference of electronegativity and atomic radii. Furthermore, the unique P – CoMo₂S₄/Co₄S₃-Co₂P heterostructure shows a superior pore volume and enhanced specific surface area of 30.4 m² g⁻¹, about 10 times higher than that of Co₂P of 3.1 m² g⁻¹ (**Fig. 2k**), thus expected to create an enriched state of exposed active sites and reasonable porous characteristic to facilitate the charge transfer and mass diffusion during electrochemical reactions.

The surface chemical state of the as-synthesized materials, including the P – CoMo₂S₄/Co₄S₃-Co₂P, CoMo₂S₄/Co₄S₃-Co₂P, and Co₄S₃-Co₂P, were identified by XPS analysis (**Fig. S5**). The high-resolution XPS (HR-XPS) Co 2p spectrum of the P – CoMo₂S₄/Co₄S₃-Co₂P can be deconvoluted into three doublets of Co³⁺ (781.6 and 797.6) eV, Co²⁺ (783.1 and 799.1) eV, and satellite component (786.4 and 803.4) eV [30]. Additionally, a doublet at binding energies of (778.5 and 793.5) eV is assigned to the characteristics of the Co–P bond (**Fig. 3a**) [31,32]. The HR-XPS Mo3d spectrum in **Fig. 3b** can be deconvoluted into two doublets of Mo⁴⁺ (230.1 and 233.2) eV and Mo⁶⁺ (232.2 and 235.4) eV, along with a peak located at 226.3 eV attributed to S–metal bond [14, 33–35]. The HR-XPS P 2p spectrum shows two peaks at binding energies of 130.2 and 130.9 eV that are attributed to P 2p_{3/2} and P 2p_{1/2} binding energies, respectively, derived from phosphide features [36],

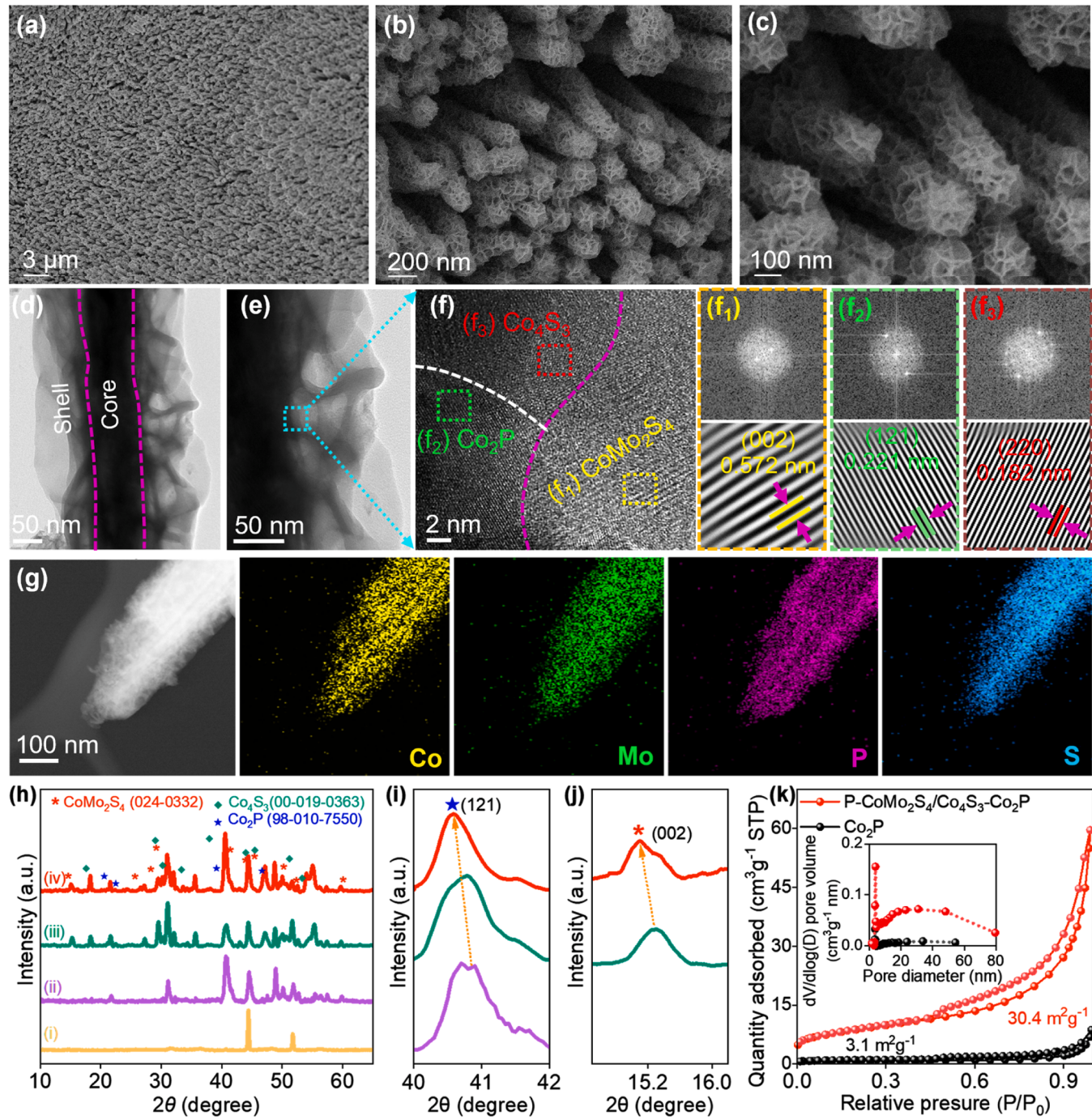


Fig. 2. (a)–(c) FE-SEM images of the P–CoMo₂S₄/Co₄S₃–Co₂P at different magnifications; (d) and (e) TEM images of P–CoMo₂S₄/Co₄S₃–Co₂P structure; (f) HR-TEM image of the P–CoMo₂S₄/Co₄S₃–Co₂P along with the corresponding area of (f₁) FFT and IFFT images of CoMo₂S₄ phase, (f₂) FFT and IFFT images of Co₂P phase, (f₃) FFT and IFFT images of Co₄S₃ phase; (g) EDS color mapping of the P–CoMo₂S₄/Co₄S₃–Co₂P structure; (h) XRD patterns of the (iv) P–CoMo₂S₄/Co₄S₃–Co₂P, (iii) CoMo₂S₄/Co₄S₃–Co₂P, (ii) Co₄S₃–Co₂P, (i) Co₂P and their corresponding high-magnification XRD patterns in the 2θ range (40–42)°; (j) CoMo₂S₄ and their corresponding high-magnification XRD patterns in the 2θ range (14.5–6.2)°; (k) Nitrogen adsorption–desorption isotherms and porous distribution of the P–CoMo₂S₄/Co₄S₃–Co₂P and Co₂P materials.

while a peak available at binding energy of 134.3 eV is attributed to the P–O bond from phosphates [32] (Fig. 3c). The HR-XPS S2p spectrum in Fig. 3d can be deconvoluted into two peaks located at 162.1 and 163.3 eV, corresponding to the S 2p_{3/2} and S 2p_{1/2} binding energies, respectively, in sulfide structures [37], while a peak appearing at binding energy of 168.6 eV corresponds to the S–O bond from sulfates [38]. Interestingly, there is a certain shift of Co 2p, Mo 3d, P 2p, and S 2p binding energies, as compared to those of other materials, indicating the charge redistribution of Co, Mo, P, and S atoms at the surface of the

CoMo₂S₄ layer, which was thereby expected to produce new electronic properties and unique catalytic behaviors toward the HER and OER processes [20,21,39]. To verify any changes caused by the above observations, we applied DFT calculations to investigate the DOS and Gibbs free energy of adsorption of hydrogen (ΔG_{H^+}) of different material models based on the as-prepared catalysts (Figs. S6 and 3e). As seen from Fig. 3f, the TDOS analysis indicates the improvement of electronic properties with the formation of core–shell heterostructure, along with the P-doping effect.

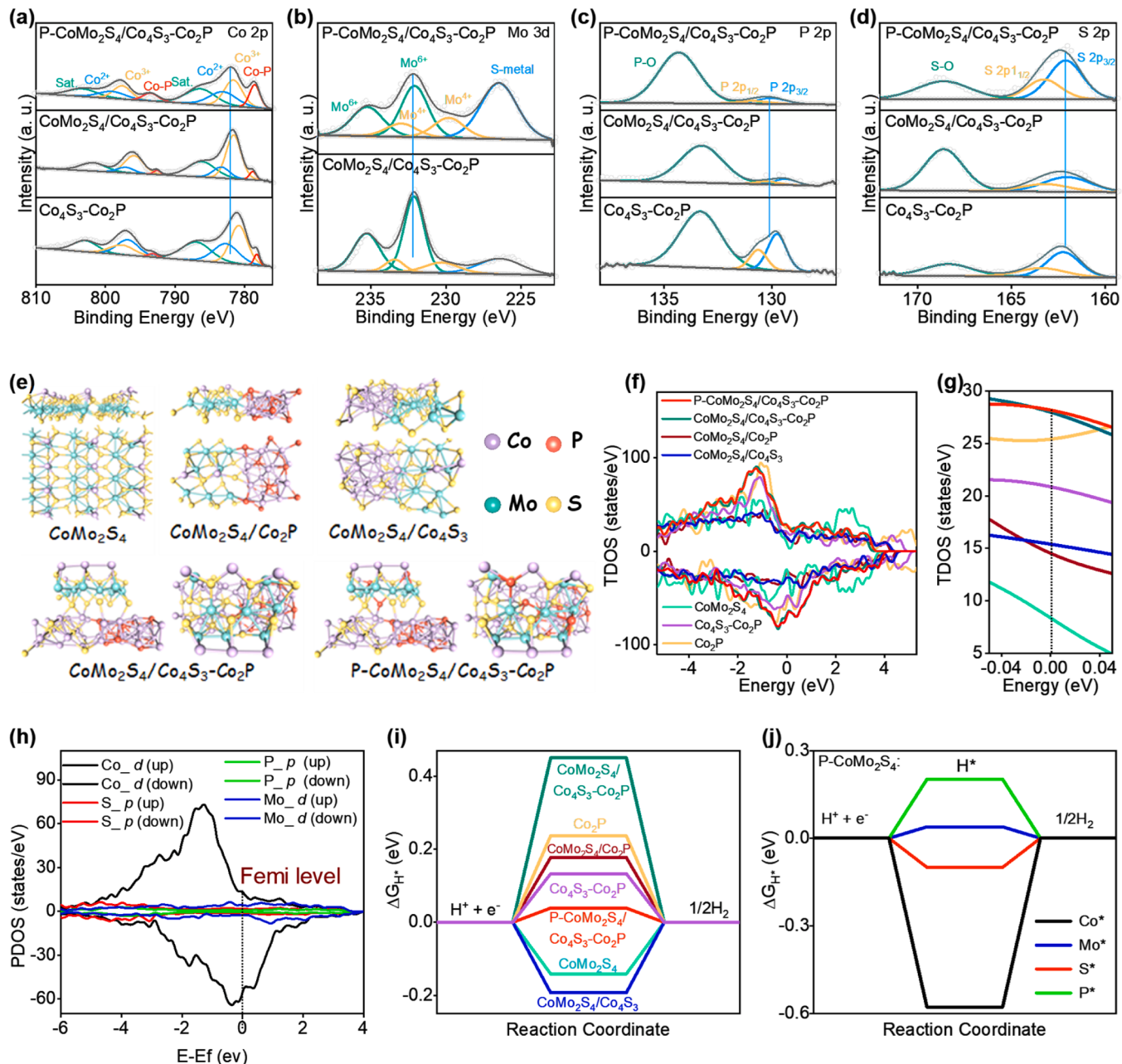


Fig. 3. HR-XPS spectra of the (a) Co 2p, (b) Mo 3d, (c) P 2p, and (d) S 2p binding energies from the P – CoMo₂S₄/Co₄S₃-Co₂P, CoMo₂S₄/Co₄S₃-Co₂P, and Co₄S₃-Co₂P materials. (e) Structural models based on the different developed materials: CoMo₂S₄, CoMo₂S₄/Co₂P, CoMo₂S₄/Co₄S₃, CoMo₂S₄/Co₄S₃-Co₂P, and P – CoMo₂S₄/Co₄S₃-Co₂P; (f) TDOS, and (g) TDOS values at near Fermi level of the different materials; (h) PDOS values of the P – CoMo₂S₄/Co₄S₃-Co₂P with different valence bands; (i) ΔG_{H^*} of the different materials; (j) ΔG_{H^*} of different atoms on surface of the P – CoMo₂S₄ shell.

The CoMo₂S₄/Co₄S₃-Co₂P and P – CoMo₂S₄/Co₄S₃-Co₂P materials exhibit a significantly high DOS value at Fermi level, as compared to the CoMo₂S₄/Co₂P, CoMo₂S₄/Co₄S₃, CoMo₂S₄, Co₄S₃-Co₂P, or Co₂P materials (Fig. 3g). In particular, the addition of certain P atoms via the doping step led to further increase of DOS value, suggesting that the P – CoMo₂S₄/Co₄S₃-Co₂P possesses the best electronic properties, with superior conductivity to promote the reaction kinetics of electrochemical processes. The exciting electronic state at near Fermi level of the P – CoMo₂S₄/Co₄S₃-Co₂P results from the contribution of the d valence band provided by Co and Mo elements (Fig. 3h). The ΔG_{H^*} behavior of different materials is also predicted in Fig. 3i, which reveals that the P – CoMo₂S₄/Co₄S₃-Co₂P can deliver a ΔG_{H^*} value of 0.0389 eV, the best thermodynamical record, as compared to that of the CoMo₂S₄/Co₄S₃-Co₂P (0.4506 eV), CoMo₂S₄/Co₄S₃ (-0.1928 eV),

CoMo₂S₄/Co₂P (0.1773 eV), CoMo₂S₄ (-0.1413 eV), Co₄S₃-Co₂P (0.1329 eV), and Co₂P (0.2367 eV). Another concern is that the most important active centers in the P – CoMo₂S₄/Co₄S₃-Co₂P structure for promoting the HER process were also predicted by allowing H-adsorption on different atoms on the surface of the P – CoMo₂S₄ shell (Fig. S7). As observed in Fig. 3j, the Mo* site shows the most favorable ΔG_{H^*} value of 0.0389 eV, followed by the S* site (-0.0996 eV), Co* site (0.2020 eV), and P* site (-0.5772 eV), suggesting that Mo atoms at the surface of the P – CoMo₂S₄/Co₄S₃-Co₂P are mainly responsible for catalyzing the HER process in alkaline medium.

3.2. Electrochemical performances

The HER performance of the different developed catalysts was

characterized by LSV technique in 1.0 M KOH electrolyte at a scan rate as 2.0 mV s⁻¹. The iR-corrected LSV curves in Fig. 4a indicate that the P – CoMo₂S₄/Co₄S₃–Co₂P has excellent current response and overpotential (η) superior to the other fabricated candidates. Specifically, to attain a current output of (10 and 100) mA cm⁻², the required η value of the P – CoMo₂S₄/Co₄S₃–Co₂P is found to be only (54 and 103) mV, respectively, significantly smaller than those of the CoMo₂S₄/Co₄S₃–Co₂P (93 and 195) mV, Co₄S₃–Co₂P (163 and 290) mV and Co₂P at (194 and 347) mV (Fig. S8). The activity of the P – CoMo₂S₄/Co₄S₃–Co₂P also surpasses those of many recently reported studies (Table S1). In particular, the P – CoMo₂S₄/Co₄S₃–Co₂P requires less η value than the commercial Pt/C catalyst since the current response is above 104 mA cm⁻². The Tafel slope is assessed to estimate the HER kinetics of the catalysts. A low Tafel slope value of 61 mV dec⁻¹ is found for the P – CoMo₂S₄/Co₄S₃–Co₂P in Fig. 4b, which is significantly lower than that of the CoMo₂S₄/Co₄S₃–Co₂P (78 mV dec⁻¹), Co₄S₃–Co₂P (108 mV dec⁻¹) and Co₂P (120 mV dec⁻¹). The results demonstrate that the HER process occurring on the surface of the P – CoMo₂S₄/Co₄S₃–Co₂P follows the Volmer–Heyrovsky route, wherein a first Heyrovsky step controls the HER rate [40]. Durability is also a critical performance to evaluate the feasibility of catalysts. Therefore, the HER stability of the P – CoMo₂S₄/Co₄S₃–Co₂P was measured by

chronoamperometry technique at two constant outputs of 10 and 100 mA cm⁻² in alkaline medium for long-term operation. Surprisingly, even after 40 h continuous testing, the catalytic performance of the P – CoMo₂S₄/Co₄S₃–Co₂P remained at 96.8% and 94.9%, respectively (Fig. 4c). In addition, the structure and morphology of the post-HER P – CoMo₂S₄/Co₄S₃–Co₂P material examined by SEM and XRD techniques in Figs S9 and S10 reveals a well-retained morphology, without significant change of crystalline features. The XPS analysis in Fig. S11 indicates the presence of binding energies corresponding to Co, Mo, P, and S elements in the post-HER sample. Some changes of surface chemistry are observed with the disappearance of the Co–P peak in the Co 2p, intensity decrease of the S 2s in the Mo 3d, P 2p_{3/2} and P 2p_{1/2} in the P 2p, and S 2p_{3/2} and S 2p_{1/2} in the S 2p (Fig. S12). Meanwhile, there is an increase of P – O in the P 2p and S–O in the S 2p, further indicating certain surface oxidation during long-term operation in aqueous electrolyte environment.

The OER activity of different developed materials, as well as the RuO₂ catalyst, was also investigated by LSV technique in alkaline solution at 2.0 mV s⁻¹. The LSV responses in Fig. 4d indicate that the P – CoMo₂S₄/Co₄S₃–Co₂P demonstrates superior OER behavior to the others. In this context, to reach (50 or 100) mA cm⁻², it needs an η value of only (296 or 311) mV, considerably better than that of the CoMo₂S₄/

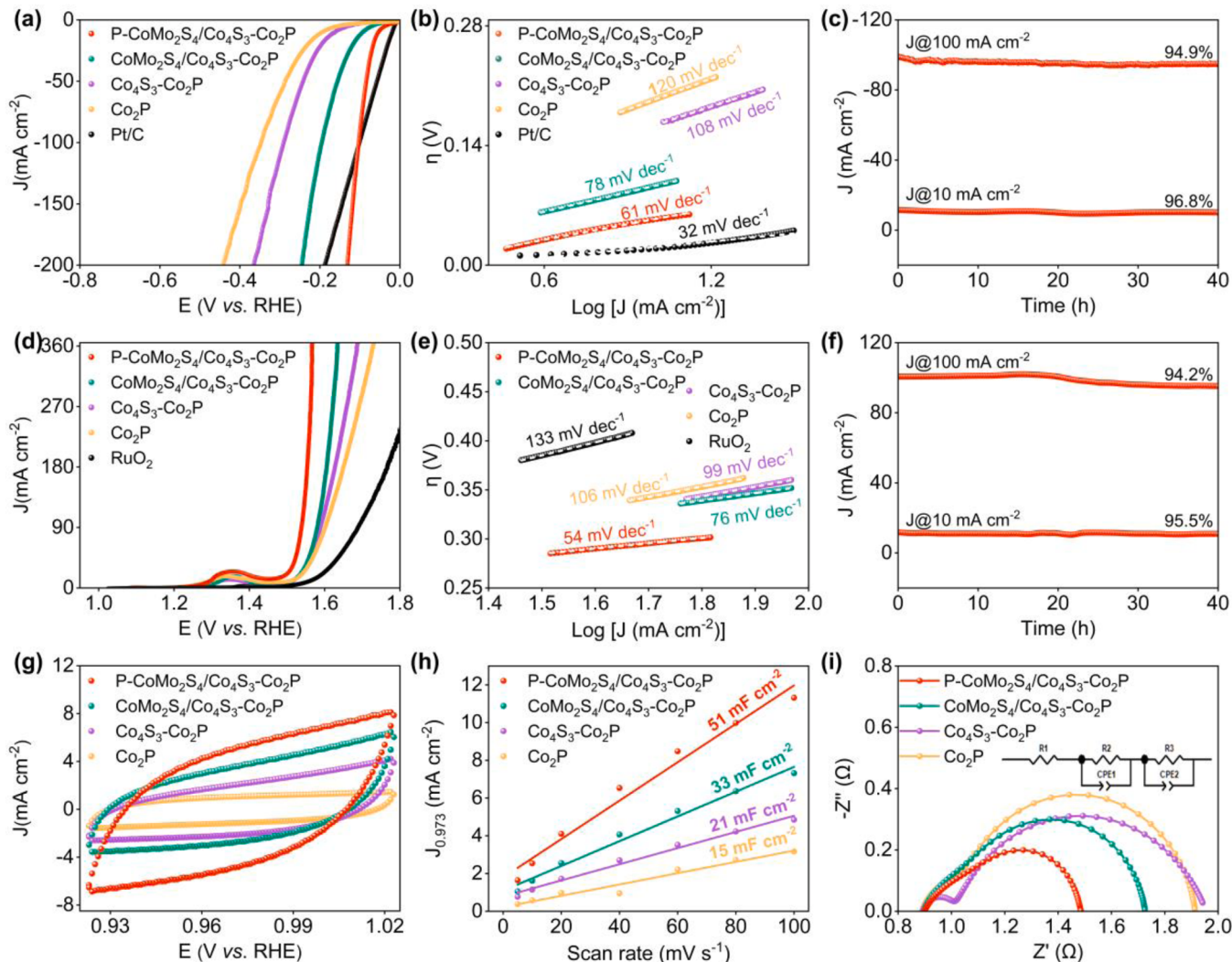


Fig. 4. (a) iR-corrected LSV responses, and (b) Tafel slopes, of the different developed materials toward HER in alkaline medium; (c) Chronoamperometric durability of the P – CoMo₂S₄/Co₄S₃–Co₂P for HER at different initial current outputs; (d) iR-corrected LSV responses, and (e) Tafel slopes, of the developed materials toward OER in alkaline medium; (f) Chronoamperometric durability of the P – CoMo₂S₄/Co₄S₃–Co₂P for OER at different initial current outputs; (g) CV responses at a sweep rate of 80 mV s⁻¹; (h) C_{dl} values, and (i) EIS results, of the developed materials, measured in the frequency range (10⁵ to 10⁻²) Hz.

$\text{Co}_4\text{S}_3-\text{Co}_2\text{P}$ (332 or 353) mV, $\text{Co}_4\text{S}_3-\text{Co}_2\text{P}$ (335 or 363) mV, Co_2P (343 or 377) mV, and commercial RuO_2 (413 or 469) mV (Fig. S13), even when compared to many recently reported studies (Table S2). Fig. 4e shows the Tafel plots of the catalysts, in which the $\text{P}-\text{CoMo}_2\text{S}_4/\text{Co}_4\text{S}_3-\text{Co}_2\text{P}$ has a lower slope of only 54 mV dec⁻¹, while the $\text{CoMo}_2\text{S}_4/\text{Co}_4\text{S}_3-\text{Co}_2\text{P}$, $\text{Co}_4\text{S}_3-\text{Co}_2\text{P}$, Co_2P , and commercial RuO_2 display a slope of 76, 99, 106, and 133 mV dec⁻¹, respectively, evidencing the excellent OER kinetics of the $\text{P}-\text{CoMo}_2\text{S}_4/\text{Co}_4\text{S}_3-\text{Co}_2\text{P}$ among all the surveyed catalyst candidates. Fig. 4f shows the long-term OER stability of the $\text{P}-\text{CoMo}_2\text{S}_4/\text{Co}_4\text{S}_3-\text{Co}_2\text{P}$ in 1.0 M KOH solution that was studied by chronoamperometric technique at initial outputs of 10 and 100 mA cm⁻², which surprisingly exhibits a respectable activity maintenance of 95.5% and 94.2%, respectively, even after continuously operating for a long-term test of 40 h, revealing the prospective stability toward OER in alkaline medium. Such achievement is also well supported by analyses of the FE-SEM and XRD techniques, which exhibit great preservation of the morphology of the original 3D hierarchical structure (Fig. S14) and invisible crystalline change (Fig. S15) for the post-OER sample. Like the HER case, XPS analysis results of the post-OER sample also reveal a certain surface oxidation at its surface (Fig. S16), as observed by the vanishing of the Co-P bond and the noticeable increase of the P-O/S-O bond (Fig. S17). Particularly, Raman analysis result of the post-OER sample in Fig. S18 further confirms that in addition to the specific Raman bands of CoMo_2S_4 structure

in the range of 200–420 cm⁻¹ [41], a peak couple appearing at (535.6 and 693.5) cm⁻¹ is resulted from the vibration modes of cobalt oxide while a peak located at 487.9 cm⁻¹ is associated with the vibration mode of CoOOH species [42]. These observations indicate the formation of active oxy(hydroxide) sites, which are highly beneficial for promoting the OER process [43–45].

The superior HER and OER performances enabled by the $\text{P}-\text{CoMo}_2\text{S}_4/\text{Co}_4\text{S}_3-\text{Co}_2\text{P}$ could be further understood by studying the electrochemical active surface area (ECSA), and charge transfer resistance (R_{ct}), of the developed catalysts. In this context, the ECSA of different materials is estimated by CV measurement at various scan rates of (5, 10, 20, 40, 60, 80, and 100 mV s⁻¹) in a non-Faraday region to obtain their double-layer capacitance (C_{dl}) (Fig. S19). The $\text{P}-\text{CoMo}_2\text{S}_4/\text{Co}_4\text{S}_3-\text{Co}_2\text{P}$ both possesses the largest integrated CV area in Fig. 4g, and demonstrates the best C_{dl} value of 51 mF cm⁻², superior to the $\text{CoMo}_2\text{S}_4/\text{Co}_4\text{S}_3-\text{Co}_2\text{P}$, $\text{Co}_4\text{S}_3-\text{Co}_2\text{P}$, and Co_2P having values of 33, 21, and 15 mF cm⁻², respectively (Fig. 4h), proving the rich active site state of the $\text{P}-\text{CoMo}_2\text{S}_4/\text{Co}_4\text{S}_3-\text{Co}_2\text{P}$ effectively promotes the catalytic reactions [27]. The intrinsic catalytic activities of the developed catalysts were also studied by the ECSA normalized-LSV curves in Figs. S20–S21, which clearly indicate the better current density and overpotential responses of $\text{P}-\text{CoMo}_2\text{S}_4/\text{Co}_4\text{S}_3-\text{Co}_2\text{P}$ towards HER and OER processes, as compared to other materials, evidencing its superior activities in alkaline medium. Another concern is that the Nyquist plots

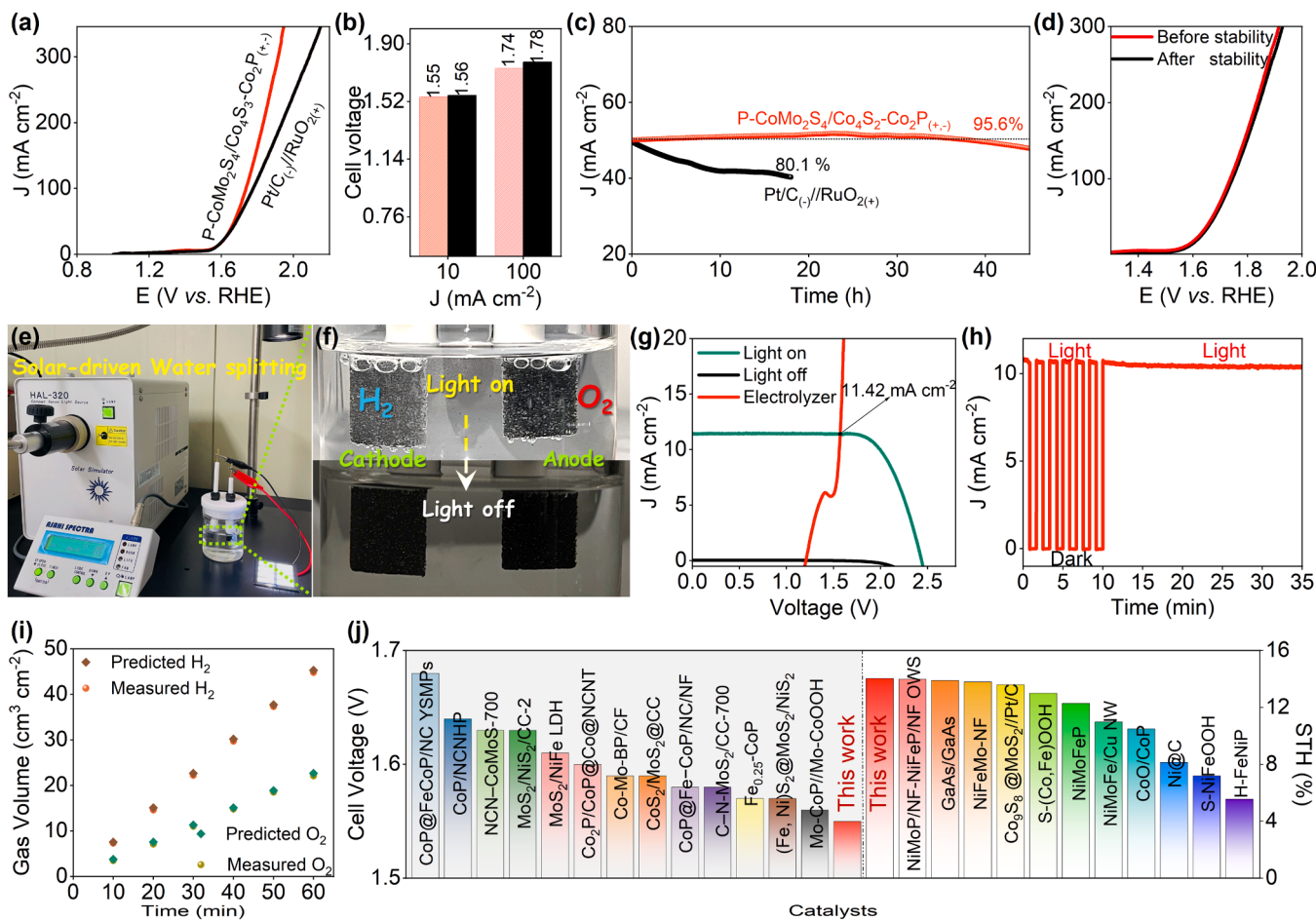


Fig. 5. (a) iR-corrected LSV responses of two electrolyzer cells based on the $\text{P}-\text{CoMo}_2\text{S}_4/\text{Co}_4\text{S}_3-\text{Co}_2\text{P}_{(+,-)}$ and $\text{Pt}/\text{C}_{(-)}/\text{RuO}_2_{(+)}$ toward alkaline water splitting, (b) A comparison of the cell voltage at 10 and 100 mA cm⁻² between $\text{P}-\text{CoMo}_2\text{S}_4/\text{Co}_4\text{S}_3-\text{Co}_2\text{P}_{(+,-)}$ and $\text{Pt}/\text{C}_{(-)}/\text{RuO}_2_{(+)}$; (c) Chronoamperometric durability of the $\text{P}-\text{CoMo}_2\text{S}_4/\text{Co}_4\text{S}_3-\text{Co}_2\text{P}_{(+,-)}$ and $\text{Pt}/\text{C}_{(-)}/\text{RuO}_2_{(+)}$ cells for 45 h water electrolysis operation; (d) LSV responses of the $\text{P}-\text{CoMo}_2\text{S}_4/\text{Co}_4\text{S}_3-\text{Co}_2\text{P}_{(+,-)}$ before stability and after durability test; (e) and (f) The solar energy-powered water electrolyzer system; (g) Response of the solar energy-powered $\text{P}-\text{CoMo}_2\text{S}_4/\text{Co}_4\text{S}_3-\text{Co}_2\text{P}_{(+,-)}$ for water splitting; (h) J-t curve of the solar energy-powered $\text{P}-\text{CoMo}_2\text{S}_4/\text{Co}_4\text{S}_3-\text{Co}_2\text{P}_{(+,-)}$ under on or off signal of irradiation. (i) Faradaic efficiency of the $\text{P}-\text{CoMo}_2\text{S}_4/\text{Co}_4\text{S}_3-\text{Co}_2\text{P}_{(+,-)}$; (j) Cell voltage and STH of the solar energy-powered $\text{P}-\text{CoMo}_2\text{S}_4/\text{Co}_4\text{S}_3-\text{Co}_2\text{P}_{(+,-)}$ are compared with those of recent works.

assessed by EIS in Fig. 4i explore a much lower R_{ct} value of the P–CoMo₂S₄/Co₄S₃–Co₂P than that of the other materials, suggesting its excellent charge transfer properties to accelerate the reaction kinetics of the electrochemical processes. In addition, the superior catalytic performance of the P–CoMo₂S₄/Co₄S₃–Co₂P also results from the highly porous architecture, which enables the exposure of a huge specific contact surface area and high pore volume for effective mass diffusion. Furthermore, the use of 3D NF foam facilitates the escape of gas products, provides excellent electrical conductivity, and promotes excellent mechanical properties for the superior stability of long-term operation during electrochemical reactions.

Inspired by the admirable catalytic performances of the P–CoMo₂S₄/Co₄S₃–Co₂P for both HER and OER processes, a two-electrode electrolyzer cell of the P–CoMo₂S₄/Co₄S₃–Co₂P_(+,-) was constructed for overall alkaline water splitting, and its efficiency was compared with the commercial Pt/C₍₋₎//RuO₂₍₊₎ coupled system. The LSV responses of the P–CoMo₂S₄/Co₄S₃–Co₂P_(+,-) in Fig. 5a exhibit superior performance, as compared to the Pt/C₍₋₎//RuO₂₍₊₎. To attain an output of (10 or 100) mA cm⁻², the CoMo₂S₄/Co₄S₃–Co₂P_(+,-) cell needs a cell voltage of just (1.55 or 1.74) V, lower than that achieved from the Pt/C₍₋₎//RuO₂₍₊₎ of (1.56 or 1.78) V, respectively (Fig. 5b). The durability of the P–CoMo₂S₄/Co₄S₃–Co₂P_(+,-) together with the Pt/C₍₋₎//RuO₂₍₊₎ cell was then examined by chronoamperometry at an initial output of 50 mA cm⁻² in Fig. 5c. The performance of the P–CoMo₂S₄/Co₄S₃–Co₂P_(+,-) cell after 45 h operation was found to remain at about 95.6%, whereas after only 10 h operation, the Pt/C₍₋₎//RuO₂₍₊₎ at the same working conditions shows a notable drop with 80.1% performance retention. In addition, the LSV curves of the P–CoMo₂S₄/Co₄S₃–Co₂P_(+,-) cell before and after stability test show minor change of overpotential and current response (Fig. 5d), evidencing the exciting durability of the P–CoMo₂S₄/Co₄S₃–Co₂P_(+,-) device for long-term operation toward the overall water splitting application. To verify the complete green production process of clean hydrogen gas via water splitting, a lab-scale solar energy-power P–CoMo₂S₄/Co₄S₃–Co₂P_(+,-) electrolyzer system was designed, which is shown in Fig. 5e. The water splitting performance of the P–CoMo₂S₄/Co₄S₃–Co₂P_(+,-) is dependent on the on/off state of simulated solar irradiation. Fig. 5f indicates that while the solar panel receives solar energy, there are abundant gas bubbles evolving from the surface of electrodes, evidencing the effective water splitting process under power supply by the solar energy source. The intersection derived from the J–V response of the solar cell under AM 1.5 G simulated sunlight and the LSV response of the electrolyzer cell reveals a value of 11.42 mA cm⁻², consistent with a solar-to-hydrogen (STH) conversion efficiency value of about 14.1% (Fig. 5g). A study of the performance of the electrolyzer for long-term operation upon the light-on or light-off signal of the solar power source in Fig. 5h indicates a fast current response, which can also maintain steady state for a long-term period of operation. The Faraday efficiency (ηF) was calculated to clarify the efficiency of the catalytic process at converting the electrical energy into the desired H₂ and O₂ gas products.

By comparing the actual amount of evolved H₂ and O₂ during the experiment and their theoretical values, the ηF value of the P–CoMo₂S₄/Co₄S₃–Co₂P_(+,-) during the water splitting process is found to be 98.9% for H₂ evolution, or 98.1% for O₂ evolution (Fig. 5i). The superior performances of the developed system in terms of cell voltage and STH efficiency are also well verified, since it is compared to the results of previous studies (Fig. 5j) [39,46–68], further demonstrating the prospective feasibility for clean hydrogen production.

4. Conclusion

In this research, we have developed a high-performance electrocatalyst based on a unique P–CoMo₂S₄/Co₄S₃–Co₂P heterostructure catalyst grown on a 3D NF substrate, which can deliver huge specific surface area with more exposed active sites, high electrical conductivity,

and excellent physical strength. These advantages enable the developed catalyst to provide excellent catalytic performance with low overpotential and excellent durability toward the HER and OER processes. At a current output of 10 mA cm⁻², the P–CoMo₂S₄/Co₄S₃–Co₂P_(+,-) electrolyzer cell could deliver a low cell voltage as small as 1.55 V, surpassing that of the Pt/C₍₋₎//RuO₂₍₊₎ couple. In addition, the solar energy-powered water electrolyzer realizes a high current density of 11.42 mA cm⁻² along with a STH efficiency of 14.1%, thus highlighting the potential applications of the P–CoMo₂S₄/Co₄S₃–Co₂P catalyst for sustainable and robust electrocatalytic water splitting, to produce clean hydrogen energy.

CRediT authorship contribution statement

Dong Kaixuan: Data curation, Formal analysis, Investigation, Validation, Writing – original draft. **Prabhakaran Sampath:** Data curation, Investigation, Writing – original draft. **Tran Duy Thanh:** Conceptualization, Data curation, Supervision, Validation, Writing – review & editing. **Kim Do Hwan:** Data curation, Software, Validation, Writing – review & editing. **Li Xue:** Data curation, Formal analysis, Investigation, Visualization. **Lee Joong Hee:** Funding acquisition, Project administration, Resources, Supervision, Writing – review & editing. **Kim Nam Hoon:** Data curation, Investigation, Supervision, Writing – review & editing.

Declaration of Competing Interest

The authors declare that they have no known competing financial interests or personal relationships that could have appeared to influence the work reported in this paper.

Data availability

Data will be made available on request.

Acknowledgements

This research was supported by the BRL (RS-2023-00207836) and the Regional Leading Research Center Program (2019R1A5A8080326) through the National Research Foundation funded by the Ministry of Science and ICT of the Republic of Korea. This work also was supported by the R&D program for Commercialization using Tech-Bridge platform (00164855) funded by the Ministry of SMEs and Startups (MSS, Korea).

Appendix A. Supporting information

Supplementary data associated with this article can be found in the online version at doi:10.1016/j.apcatb.2023.123649.

References

- [1] R. Lindner, Green hydrogen partnerships with the Global South. Advancing an energy justice perspective on “tomorrow’s oil, Sustain. Dev. 31 (2022) 1038–1053, <https://doi.org/10.1002/sd.2439>.
- [2] Z. Li, M. Hu, P. Wang, J. Liu, J. Yao, C. Li, Heterojunction catalyst in electrocatalytic water splitting, Coord. Chem. Rev. 439 (2021), 213953, <https://doi.org/10.1016/j.ccr.2021.213953>.
- [3] J. Zhu, L. Hu, P. Zhao, L.Y.S. Lee, K.Y. Wong, Recent advances in electrocatalytic hydrogen evolution using nanoparticles, Chem. Rev. 120 (2020) 851–918, <https://doi.org/10.1021/acs.chemrev.9b00248>.
- [4] Y. Luo, Z. Zhang, M. Chhowalla, B. Liu, Recent advances in design of electrocatalysts for high-current-density water splitting, Adv. Mater. 34 (2022), 2108133, <https://doi.org/10.1002/adma.202108133>.
- [5] X. Liang, C.-M.L. Wu, Metal-free two-dimensional phosphorus carbide as an efficient electrocatalyst for hydrogen evolution reaction comparable to platinum, Nano Energy 71 (2020), <https://doi.org/10.1016/j.nanoen.2020.104603>.
- [6] T.D. Thanh, N.D. Chuong, H.V. Hien, T. Kshetri, L.H. Tuan, N.H. Kim, J.H. Lee, Recent advances in two-dimensional transition metal dichalcogenides-graphene heterostructured materials for electrochemical applications, Prog. Mater. Sci. 96 (2018) 51–85, <https://doi.org/10.1016/j.pmatsci.2018.03.007>.

- [7] L. Han, S. Dong, E. Wang, Transition-Metal (Co, Ni, and Fe)-Based Electrocatalysts for the Water Oxidation Reaction, *Adv. Mater.* 28 (2016) 9266–9291, <https://doi.org/10.1002/adma.201602270>.
- [8] J. Wang, F. Xu, H. Jin, Y. Chen, Y. Wang, Non-Noble Metal-based Carbon Composites in Hydrogen Evolution Reaction: Fundamentals to Applications, *Adv. Mater.* 29 (2017), 1605838, <https://doi.org/10.1002/adma.201605838>.
- [9] B. Ren, H. Cui, C. Wang, Self-supported graphene nanosheet-based composites as binder-free electrodes for advanced electrochemical energy conversion and storage, *Electrochem. Energy Rev.* 5 (2022), 32, <https://doi.org/10.1007/s41918-022-00138-6>.
- [10] S. Lalwani, M. AlNahyan, A. Al Zaabi, F. AlMarzooqi, A. Qurashi, Developments and perspectives on robust nano-and microstructured binder-free electrodes for bifunctional water electrolysis and beyond, *Adv. Energy Mater.* 12 (2022), 2200409, <https://doi.org/10.1002/aenm.202200409>.
- [11] H. Sun, Z. Yan, F. Liu, W. Xu, F. Cheng, J. Chen, Self-supported transition-metal-based electrocatalysts for hydrogen and oxygen evolution, *Adv. Mater.* 32 (2020), 1806326, <https://doi.org/10.1002/adma.201806326>.
- [12] J. Kwon, H. Han, S. Choi, K. Park, S. Jo, U. Paik, T. Song, Current status of self-supported catalysts for robust and efficient water splitting for commercial electrolyzer, *ChemCatChem* 11 (2019) 5898–5912, <https://doi.org/10.1002/cctc.201901638>.
- [13] P.K.L. Tran, D.T. Tran, M. Austeria P, D.H. Kim, N.H. Kim, J.H. Lee, Intermolecular Metallic Single-Site Complexes Dispersed on Mo₂TiC₂T_x/MoS₂ Heterostructure Induce Boosted Solar-Driven Water Splitting, *Adv. Energy Mater.* 13 (2023), 2203844, <https://doi.org/10.1002/aenm.202203844>.
- [14] Y. Guo, J. Tang, J. Henzie, B. Jiang, W. Xia, T. Chen, Y. Bando, Y.M. Kang, M.S. A. Hossain, Y. Sugahara, Y. Yamauchi, Mesoporous Iron-doped MoS₂/CoMo₂S₄ Heterostructures through Organic-Metal Cooperative Interactions on Spherical Micelles for Electrochemical Water Splitting, *ACS Nano* 14 (2020) 4141–4152, <https://doi.org/10.1021/acsnano.9b08904>.
- [15] H. Cheng, Q. Liu, Y. Diao, L. Wei, J. Chen, F. Wang, CoMo₂S₄ with Superior Conductivity for Electrocatalytic Hydrogen Evolution: Elucidating the Key Role of Co, *Adv. Funct. Mater.* 31 (2021) 20210372, <https://doi.org/10.1002/adfm.202103732>.
- [16] C. Huang, L. Yu, W. Zhang, Q. Xiao, J. Zhou, Y. Zhang, P. An, J. Zhang, Y. Yu, N-doped Ni-Mo based sulfides for high-efficiency and stable hydrogen evolution reaction, *Appl. Catal. B-Environ.* 276 (2020), 119137, <https://doi.org/10.1016/j.apcatb.2020.119137>.
- [17] C. Yang, L. Zhou, T. Yan, Y. Bian, Y. Hu, C. Wang, Y. Zhang, Y. Shi, D. Wang, Y. Zhen, F. Fu, Synergistic mechanism of Ni(OH)₂/NiMoS heterostructure electrocatalyst with crystalline/amorphous interfaces for efficient hydrogen evolution over all pH ranges, *J. Colloid Interface Sci.* 606 (2022) 1004–1013, <https://doi.org/10.1016/j.jcis.2021.08.090>.
- [18] Y. Xue, X. Bai, Y. Xu, Q. Yan, M. Zhu, K. Zhu, K. Ye, J. Yan, D. Cao, G. Wang, Vertically oriented Ni-doped MoS₂ nanosheets supported on hollow carbon microtubes for enhanced hydrogen evolution reaction and water splitting, *Compos. Part B-Eng.* 224 (2021), 109229, <https://doi.org/10.1016/j.compositesb.2021.109229>.
- [19] V.R. Jothi, K. Karuppasamy, T. Maiyalagan, H. Rajan, C.Y. Jung, S.C. Yi, Corrosion and Alloy Engineering in Rational Design of High Current Density Electrodes for Efficient Water Splitting, *Adv. Energy Mater.* 10 (2020), 190420, <https://doi.org/10.1002/aenm.201904020>.
- [20] Z. Zheng, L. Yu, M. Gao, X. Chen, W. Zhou, C. Ma, L. Wu, J. Zhu, X. Meng, J. Hu, Y. Tu, S. Wu, J. Mao, Z. Tian, D. Deng, Boosting hydrogen evolution on MoS(2) via co-confining selenium in surface and cobalt in inner layer, *Nat. Commun.* 11 (2020), 3315, <https://doi.org/10.1038/s41467-020-17199-0>.
- [21] Q. Jin, N. Liu, C. Dai, R. Xu, B. Wu, G. Yu, B. Chen, Y. Du, H₂-Directing Strategy on In Situ Synthesis of Co-MoS₂ with Highly Expanded Interlayer for Elegant HER Activity and its Mechanism, *Adv. Energy Mater.* 10 (2020), 2000291, <https://doi.org/10.1002/aenm.202000291>.
- [22] Y. Song, W. Sha, T. Jiao, C. Wang, J. Tian, P. Liu, B. Xu, J. Guo, J. Liang, Interface-engineered Co₃S₄/CoMo₂S₄ nanosheets as efficient bifunctional electrocatalysts for alkaline overall water splitting, *Nanotechnology* 32 (2021), 455706, <https://doi.org/10.1088/1361-6528/ac1a41>.
- [23] D.C. Nguyen, D.T. Tran, T.L.L. Doan, D.H. Kim, N.H. Kim, J.H. Lee, Rational Design of Core@shell Structured CoS_x@Cu₂MoS₄ Hybridized MoS₂/N,S-Codoped Graphene as Advanced Electrocatalyst for Water Splitting and Zn-Air Battery, *Adv. Energy Mater.* 10 (2020), 1903289, <https://doi.org/10.1002/aenm.201903289>.
- [24] H. Su, S. Song, S. Li, Y. Gao, L. Ge, W. Song, T. Ma, J. Liu, High-valent bimetal Ni₃S₂/Co₃S₄ induced by Cu doping for bifunctional electrocatalytic water splitting, *Appl. Catal. B-Environ.* 293 (2021), 120225, <https://doi.org/10.1016/j.apcatb.2021.120225>.
- [25] D. Jin, F. Qiao, W. Liu, Y. Liu, Y. Xie, H. Li, One-step fabrication of MoS₂/Ni₃S₂ with P-doping for efficient water splitting, *CrystEngComm* 24 (2022) 4057–4062, <https://doi.org/10.1039/dce00493c>.
- [26] Y. Guo, X. Zhou, J. Tang, S. Tanaka, Y.V. Kaneti, J. Na, B. Jiang, Y. Yamauchi, Y. Bando, Y. Sugahara, Multiscale structural optimization: Highly efficient hollow iron-doped metal sulfide heterostructures as bifunctional electrocatalysts for water splitting, *Nano Energy* 75 (2020), 104913, <https://doi.org/10.1016/j.nanoen.2020.104913>.
- [27] C.C. Gudal, U.N. Pan, D.R. Paudel, M.R. Kandel, N.H. Kim, J.H. Lee, Bifunctional P-Intercalated and Doped Metallic (1T)-Copper Molybdenum Sulfide Ultrathin 2D-Nanosheets with Enlarged Interlayers for Efficient Overall Water Splitting, *ACS Appl. Mater. Inter.* (2022) 14492–14503, <https://doi.org/10.1021/acsami.2c00278>.
- [28] M. Wang, Z. Wan, X.Y. Meng, Z.H. Li, X.G. Ding, P. Li, C. Li, J.G. Wang, Z. Li, Heterostructured Co/Mo-sulfide catalyst enables unbiased solar water splitting by integration with perovskite solar cells, *Appl. Catal. B-Environ.* 309 (2022), 121272, <https://doi.org/10.1016/j.apcatb.2022.121272>.
- [29] J. Li, G. Zheng, One-Dimensional Earth-Abundant Nanomaterials for Water-Splitting Electrocatalysts, *Adv. Sci. (Weinh.)* 4 (2017), 1600380, <https://doi.org/10.1002/advs.201600380>.
- [30] K. Chang, D.T. Tran, J. Wang, K. Dong, S. Prabhakaran, D.H. Kim, N.H. Kim, J. H. Lee, Triphasic Ni₂P–Fe₂P–CoP heterostructure interfaces for efficient overall water splitting powered by solar energy, *Appl. Catal. B-Environ.* 338 (2023), 123016, <https://doi.org/10.1016/j.apcatb.2023.123016>.
- [31] G. Li, L. Li, Z. Lin, CoP-anchored high N-doped carbon@graphene sheet as bifunctional electrocatalyst for efficient overall water splitting, *Int. J. Hydrog. Energ.* 46 (2021) 18224–18232, <https://doi.org/10.1016/j.ijhydene.2021.02.219>.
- [32] F. Zhang, X. Wang, W. Han, Y. Qian, L. Qiu, Y. He, L. Lei, X. Zhang, The Synergistic Activation of Ce-Doping and CoP/Ni₃P Hybrid Interaction for Efficient Water Splitting at Large-Current-Density, *Adv. Funct. Mater.* 33 (2022), 2212381, <https://doi.org/10.1002/adfm.202212381>.
- [33] Z. Shi, K. Nie, Z.-J. Shao, B. Gao, H. Lin, H. Zhang, B. Liu, Y. Wang, Y. Zhang, X. Sun, X.-M. Cao, P. Hu, Q. Gao, Y. Tang, Phosphorus-Mo₂C@carbon nanowires toward efficient electrochemical hydrogen evolution: composition, structural and electronic regulation, *Energ. Environ. Sci.* 10 (2017) 1262–1271, <https://doi.org/10.1039/c7ee00388a>.
- [34] L. Chen, Z. Deng, Z. Chen, X. Wang, Building Ni₉S₈/MoS₂ Nanosheets Decorated NiMoO₄ Nanorods Heterostructure for Enhanced Water Splitting, *Adv. Mater. Interfaces* 8 (2021), 2101483, <https://doi.org/10.1002/admi.202101483>.
- [35] Y.-T. Ho, C.-H. Ma, T.-T. Luong, L.-L. Wei, T.-C. Yen, W.-T. Hsu, W.-H. Chang, Y.-C. Chu, Y.-Y. Tu, K.P. Pande, E.Y. Chang, Layered MoS₂ grown on c-sapphire by pulsed laser deposition, *Phys. Status Solidi-R.* 9 (2015) 187–191, <https://doi.org/10.1002/psr.201409561>.
- [36] K. Ge, Y. Zeng, G. Dong, L. Zhao, Z. Wang, M. Huang, 3D self-standing grass-like cobalt phosphide vesicles-decorated nanocones grown on Ni-foam as an efficient electrocatalyst for hydrogen evolution reaction, *Int. J. Hydrog. Energ.* 44 (2019) 13490–13501, <https://doi.org/10.1016/j.ijhydene.2019.04.030>.
- [37] J.-G. Li, K. Xie, H. Sun, Z. Li, X. Ao, Z. Chen, K.K. Ostrikov, C. Wang, W. Zhang, Template-Directed Bifunctional Dodecahedral CoP/CN@MoS₂ Electrocatalyst for High Efficient Water Splitting, *ACS Appl. Mater. Inter.* 11 (2019) 36649–36657, <https://doi.org/10.1021/acsami.9b11859>.
- [38] Y. Hu, H. Yu, L. Qi, J. Dong, P. Yan, T. Taylor Isimjan, X. Yang, Interface Engineering of Needle-Like P-Doped MoS₂/CoP Arrays as Highly Active and Durable Bifunctional Electrocatalyst for Overall Water Splitting, *ChemSusChem* 14 (2021) 1565–1573, <https://doi.org/10.1002/cssc.202002873>.
- [39] C. Guan, W. Xiao, H. Wu, X. Liu, W. Zang, H. Zhang, J. Ding, Y.P. Feng, S. J. Pennycook, J. Wang, Hollow Mo-doped CoP nanoarrays for efficient overall water splitting, *Nano Energy* 48 (2018) 73–80, <https://doi.org/10.1016/j.nanoen.2018.03.034>.
- [40] G. Wang, J. Huang, G. Chen, W. Chen, C. Song, M. Li, X. Wang, D. Chen, H. Zhu, X. Zhang, K.K. Ostrikov, In-Situ-Engineered 3D Cu₃Se₂@CoSe₂–NiSe₂ Nanostructures for Highly Efficient Electrocatalytic Water Splitting, *ACS Sustain. Chem. Eng.* 8 (2020) 17215–17224, <https://doi.org/10.1021/acssuschemeng.0c05985>.
- [41] Y. Zhu, J. Yao, L. Bai, W. Zhang, W. Wang, X. Ma, L. Wu, Dense MoS₂/CoS₂ Heterointerfaces with Optimized Electronic Structure for Efficient Alkaline Hydrogen Evolution Reaction, *ACS Appl. Energy Mater.* 6 (2023) 2479–2488, <https://doi.org/10.1021/acsma.2c03917>.
- [42] W.H. Lee, M.H. Han, Y.-J. Ko, B.K. Min, K.H. Chae, H.-S. Oh, Electrode reconstruction strategy for oxygen evolution reaction: maintaining Fe-CoOOH phase with intermediate-spin state during electrolysis, *Nat. Commun.* 13 (2022), 605, <https://doi.org/10.1038/s41467-022-28260-5>.
- [43] J. Chen, B. Ren, H. Cui, C. Wang, Constructing pure phase tungsten-based bimetallic carbide nanosheet as an efficient bifunctional electrocatalyst for overall water splitting, *Small* 16 (2020), 1907556, <https://doi.org/10.1002/smll.201907556>.
- [44] Q. Fu, T. Wu, G. Fu, T. Gao, J. Han, T. Yao, Y. Zhang, W. Zhong, X. Wang, B. Song, *ACS Energy Lett.* 3 (2018) 1744–1752, <https://doi.org/10.1021/acsenergylett.8b00908>.
- [45] Y. Lu, X. Zheng, Y. Liu, J. Zhu, D. Li, D. Jiang, Synergistically Coupled CoMo/CoMoP Electrocatalyst for Highly Efficient and Stable Overall Water Splitting, *Inorg. Chem.* 61 (2022) 8328–8338, <https://doi.org/10.1021/acs.inorgchem.2c00923>.
- [46] H. Roh, H. Jung, H. Choi, J.W. Han, T. Park, S. Kim, K. Yong, Various metal (Fe, Mo, V, Co)-doped Ni₂P nanowire arrays as overall water splitting electrocatalysts and their applications in unassisted solar hydrogen production with STH 14, , *Appl. Catal. B-Environ.* 297 (2021), 120434, <https://doi.org/10.1016/j.apcatb.2021.120434>.
- [47] M. Baek, G.-W. Kim, T. Park, K. Yong, NiMoFe and NiMoFeP as Complementary Electrocatalysts for Efficient Overall Water Splitting and Their Application in PV-Electrolysis with STH 12.3, *Small* 15 (2019), 1905501, <https://doi.org/10.1002/smll.201905501>.
- [48] X. Cao, R. Fan, J. Zhou, C. Chen, S. Xu, S. Zou, W. Dong, X. Su, S. Ju, M. Shen, NiMoFe/Cu nanowire core-shell catalysts for high-performance overall water splitting in neutral electrolytes, *Chem. Commun.* 58 (2022) 1569–1572, <https://doi.org/10.1039/DCC06409F>.
- [49] J. Ekspont, C. Larsen, J. Stenberg, W.L. Kwong, J. Wang, J. Zhang, E.M. J. Johansson, J. Messinger, L. Edman, T. Wågberg, Solar-Driven Water Splitting at 13.8% Solar-to-Hydrogen Efficiency by an Earth-Abundant Electrolyzer, *ACS*

- Sustain. Chem. Eng. 9 (2021) 14070–14078, <https://doi.org/10.1021/acssuschemeng.1c03565>.
- [50] C. Kim, S. Lee, S.H. Kim, I. Kwon, J. Park, S. Kim, J.-h Lee, Y.S. Park, Y. Kim, Promoting electrocatalytic overall water splitting by sulfur incorporation into CoFe-(oxy)hydroxide, Nanoscale Adv. 3 (2021) 6386–6394, <https://doi.org/10.1039/D1NA00486G>.
- [51] Q.-T. Ngo, O. Omelianovych, V.-T. Nguyen, B.T. Ahn, K.-B. Lee, G.-J. Lee, L. L. Larina, H.-S. Choi, An economically sustainable bifunctional Ni@C catalyst in a solar-to-hydrogen device employing a CIGS submodule, J. Mater. Chem. A. 9 (2021) 23828–23840, <https://doi.org/10.1039/D1TA03474J>.
- [52] C. Kim, S.H. Kim, S. Lee, I. Kwon, S.H. Kim, S. Kim, C. Seok, Y.S. Park, Y. Kim, Boosting overall water splitting by incorporating sulfur into NiFe (oxy)hydroxide, J. Energy Chem. 64 (2022) 364–371, <https://doi.org/10.1016/j.jecchem.2021.04.067>.
- [53] Q. Li, Y. Wang, J. Zeng, Q. Wu, Q. Wang, L. Sun, L. Xu, T. Ye, X. Zhao, L. Chen, Z. Chen, L. Chen, Y. Lei, Phosphating-induced charge transfer on CoO/CoP interface for alkaline H₂ evolution, Chin. Chem. Lett. 32 (2021) 3355–3358, <https://doi.org/10.1016/j.cclet.2021.03.063>.
- [54] R. Zhang, G. Wang, Z. Wei, X. Teng, J. Wang, J. Miao, Y. Wang, F. Yang, X. Zhu, C. Chen, E. Zhou, W. Hu, X. Sun, A Fe–Ni₅P₄/Fe–Ni₂P heterojunction electrocatalyst for highly efficient solar-to-hydrogen generation, J. Mater. Chem. A. 9 (2021) 1221–1229, <https://doi.org/10.1039/D0TA08631B>.
- [55] Z.N. Zahran, Y. Miseki, E.A. Mohamed, Y. Tsubonouchi, K. Makita, T. Sugaya, K. Sayama, M. Yagi, Perfect Matching Factor between a Customized Double-Junction GaAs Photovoltaic Device and an Electrolyzer for Efficient Solar Water Splitting, ACS Appl. Energy Mater. 5 (2022) 8241–8253, <https://doi.org/10.1021/acsam.2c00768>.
- [56] M. Wang, Z. Wan, X. Meng, Z. Li, X. Ding, P. Li, C. Li, J.-G. Wang, Z. Li, Heterostructured Co/Mo-sulfide catalyst enables unbiased solar water splitting by integration with perovskite solar cells, Appl. Catal. B-Environ. 309 (2022), 121272, <https://doi.org/10.1016/j.apcatb.2022.121272>.
- [57] Y. Pan, K. Sun, S. Liu, X. Cao, K. Wu, W.C. Cheong, Z. Chen, Y. Wang, Y. Li, Y. Liu, D. Wang, Q. Peng, C. Chen, Y. Li, Core-Shell ZIF-8@ZIF-67-Derived CoP Nanoparticle-Embedded N-Doped Carbon Nanotube Hollow Polyhedron for Efficient Overall Water Splitting, J. Am. Chem. Soc. 140 (2018) 2610–2618, <https://doi.org/10.1021/jacs.7b12420>.
- [58] Z. Lu, Y. Cao, J. Xie, J. Hu, K. Wang, D. Jia, Construction of Co₂P/CoP@Co@NCNT rich-interface to synergistically promote overall water splitting, Chem. Eng. J. 430 (2022), 132877, <https://doi.org/10.1016/j.cej.2021.132877>.
- [59] J. Shi, F. Qiu, W. Yuan, M. Guo, Z.-H. Lu, Nitrogen-doped carbon-decorated yolk-shell CoP@FeCoP micro-polyhedra derived from MOF for efficient overall water splitting, Chem. Eng. J. 403 (2021), 126321, <https://doi.org/10.1016/j.cej.2020.126312>.
- [60] Q. Yang, H. Dai, W. Liao, X. Tong, Y. Fu, M. Qian, T. Chen, Construction of Fe-doped CoP with hybrid nanostructures as a bifunctional catalyst for overall water splitting, Dalton. T. 50 (2021) 18069–18076, <https://doi.org/10.1039/didt03292e>.
- [61] X.-P. Li, L.-R. Zheng, S.-J. Liu, T. Ouyang, S. Ye, Z.-Q. Liu, Heterostructures of NiFe LDH hierarchically assembled on MoS₂ nanosheets as high-efficiency electrocatalysts for overall water splitting, Chin. Chem. Lett. 33 (2022) 4761–4765, <https://doi.org/10.1016/j.ccl.2021.12.095>.
- [62] G. Zhou, X. Wu, M. Zhao, H. Pang, L. Xu, J. Yang, Y. Tang, Interfacial Engineering-Triggered Bifunctionality of CoS(2)/MoS(2) Nanocubes/Nanosheet Arrays for High-Efficiency Overall Water Splitting, ChemSusChem 14 (2021) 699–708, <https://doi.org/10.1002/cssc.202002338>.
- [63] M. Kim, H. Seok, N. Clament Sagaya Selvam, J. Cho, G.H. Choi, M.G. Nam, S. Kang, T. Kim, P.J. Yoo, Kirkendall effect induced bifunctional hybrid electrocatalyst (Co₃S₈@MoS₂/N-doped hollow carbon) for high performance overall water splitting, J. Power Sources 493 (2021), 229688, <https://doi.org/10.1016/j.jpowsour.2021.229688>.
- [64] J. Xu, J. Rong, Y. Zheng, Y. Zhu, K. Mao, Z. Jing, T. Zhang, D. Yang, F. Qiu, Construction of sheet-on-sheet hierarchical MoS₂/NiS₂ heterostructures as efficient bifunctional electrocatalysts for overall water splitting, Electrochim. Acta 385 (2021), 138438, <https://doi.org/10.1016/j.electacta.2021.138438>.
- [65] L. Tong, Y. Liu, C. Song, Y. Zhang, S.S. Latthe, S. Liu, R. Xing, Fe, Ni)S₂@MoS₂/NiS₂ hollow heterostructure nanocubes for high-performance alkaline water electrolysis, Int. J. Hydrog. Energ. 47 (2022) 11143–11152, <https://doi.org/10.1016/j.ijhydene.2022.01.161>.
- [66] Y. Mei, Y. Cong, S. Huang, J. Qian, J. Ye, T.T. Li, MOF-on-MOF Strategy to Construct a Nitrogen-Doped Carbon-Incorporated CoP@Fe-CoP Core-Shelled Heterostructure for High-Performance Overall Water Splitting, Inorg. Chem. 61 (2022) 1159–1168, <https://doi.org/10.1021/acs.inorgchem.1c03498>.
- [67] Y. Wei, P. Zou, Y. Yue, M. Wang, W. Fu, S. Si, L. Wei, X. Zhao, G. Hu, H.L. Xin, One-Pot Synthesis of B/P-Codoped Co-Mo Dual-Nanowafers Electrocatalysts for Overall Water Splitting, ACS Appl. Mater. Inter. 13 (2021) 20024–20033, <https://doi.org/10.1021/acsami.1c01341>.
- [68] W. Chen, W. Wei, K. Wang, J. Cui, X. Zhu, K.K. Ostrikov, Partial sulfur vacancies created by carbon-nitrogen deposition of MoS(2) for high-performance overall electrocatalytic water splitting, Nanoscale 13 (2021) 14506–14517, <https://doi.org/10.1039/d1nr02966e>.